Research

Author for correspondence:
Haimin Yao
e-mail: mmhyao@polyu.edu.hk

THE ROYAL SOCIETY
PUBLISHING

Combat biofouling with microscopic ridge-like surface morphology: a bioinspired study

Jimin Fu[1], Hua Zhang[1,2], Zhenbin Guo[1], Dan-qing Feng[3], Vengatesen Thiyagarajan[4] and Haimin Yao[1]

[1]Department of Mechanical Engineering, The Hong Kong Polytechnic University, Hung Hom, Kowloon, Hong Kong SAR, People's Republic of China
[2]Department of Chemistry and Chemical Engineering, Jiangxi Normal University, Nanchang 330022, People's Republic of China
[3]State-Province Joint Engineering Laboratory of Marine Bioproducts and Technology, College of Ocean and Earth Sciences, Xiamen University, Xiamen 361005, People's Republic of China
[4]The Swire Institute of Marine Sciences and School of Biological Sciences, The University of Hong Kong, Hong Kong SAR, People's Republic of China

JF, 0000-0003-2591-9198; HZ, 0000-0002-5587-2119; ZG, 0000-0003-0843-3612; VT, 0000-0002-2062-4799; HY, 0000-0003-0549-2246

Biofouling refers to the unfavourable attachment and accumulation of marine sessile organisms (e.g. barnacles, mussels and tubeworms) on the solid surfaces immersed in ocean. The enormous economic loss caused by biofouling in combination with the severe environmental impacts induced by the current antifouling approaches entails the development of novel antifouling strategies with least environmental impact. Inspired by the superior antifouling performance of the leaves of mangrove tree *Sonneratia apetala*, here we propose to combat biofouling by using a surface with microscopic ridge-like morphology. Settlement tests with tubeworm larvae on polymeric replicas of *S. apetala* leaves confirm that the microscopic ridge-like surface morphology can effectively prevent biofouling. A contact mechanics-based model is then established to quantify the dependence of tubeworm settlement on the structural features of the microscopic ridge-like morphology, giving rise to theoretical guidelines to optimize the morphology for better antifouling performance. Under the direction of the obtained guidelines, a synthetic surface with microscopic ridge-like morphology is developed, exhibiting antifouling performance comparable to that of the *S. apetala* replica. Our results not only reveal the underlying mechanism accounting for the superior antifouling property of the *S. apetala* leaves, but also provide applicable guidance for the development of synthetic antifouling surfaces.

1. Introduction

Marine biofouling refers to the accumulation of biomolecules and organisms on surfaces of submerged structures in ocean [1–4]. It not only affects the appearance of the structures but also causes a range of substantial impairments to marine industry, including increasing frictional drag of ships [2], smothering oceanographic equipment [5] and accelerating structural deterioration [6]. Traditional approaches to tackling marine biofouling mainly applied paints incorporated with inorganic and organometallic biocides (e.g. copper compounds and tributyltin (TBT) compounds) [7]. However, many biocides have severe negative impacts on ecology and environment. For example, TBT compounds were found to cause defective growth of mollusc shells and debilitation of immunological defence in fishes [8,9]; therefore the use of TBT in antifouling paints has been banned since the early stage of the twenty-first century. As to the copper-based paints, even though their toxicity was claimed less than that of the TBT-based ones, there are still doubts concerning the effects of high copper concentration on certain marine organisms [10]. To lower the impact of antifouling paints on
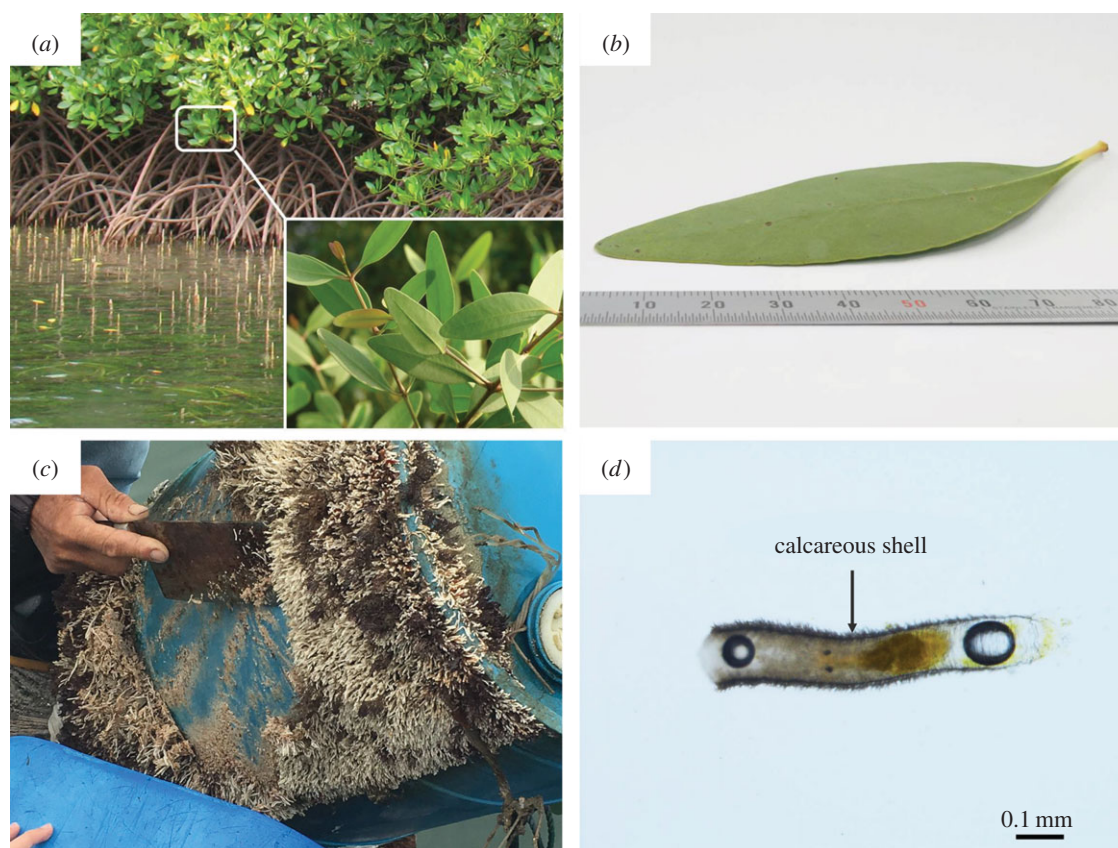
Figure 1. The antifouling leaves of *S. apetala* and tubeworm *H. elegans*. (*a*) *Sonneratia apetala* living in intertidal zone. (*b*) A leaf of *S. apetala*. (*c*) Adult tubeworms *H. elegans* accumulated on a plastic bucket. (*d*) A larva of *H. elegans* with calcareous shell.

environment, organic biocides were adopted whose toxicity is still under scrutiny [11]. Developing antifouling strategies with least environmental impact is still required.

In nature, many animals and plants have evolved surfaces with excellent antifouling competence. Inspired by these natural antifouling surfaces [12,13], researchers have devoted themselves to the development of biomimetic chemical antifoulants such as enzymes [14] and metabolites isolated from marine microorganisms[15]. However, there are still challenges for the application of these biomimetic antifoulants including high cost, short-term efficacy and specificity. In addition to chemistry, structural traits of materials such as surface morphology were also found to play an important role in preventing biofouling [16–20]. For instance, surfaces with micropattern mimicking sharkskin were found effective in prohibiting the settlement of zoospores and cyprids [20]. A polymer coating with surface topography mimicking that of the skin of pilot whale *Globicephala melas* was found capable of reducing the settlement strength of *Ulva* zoospores [21]. Apart from animals, plants can also serve as paradigms for developing biomimetic antifouling surfaces. For instance, a replica of *Trifolium* leaf was proven to inhibit settlement of microalgae and facilitate cell release [22]. Recently, mangrove tree *Sonneratia apetala* (figure 1*a*) has attracted much attention for its unique leaves. As an intertidal plant, *S. apetala* is subject to marine fouling. Interestingly, the leaves of *S. apetala*, compared to its twigs and barks, are almost immune to biofouling. Proposed mechanisms accounting for such excellent antifouling property include low surface wettability, antifoulant of oleanolic acid and post-settlement detachment [23]. However, these may not be the most dominant mechanism because leaves of other mangrove species also share these mechanisms but exhibit much worse antifouling performance

[23]. Here, we propose surface morphology as the dominant mechanism for the extraordinary antifouling competence of *S. apetala* leaves. To verify this hypothesis, we firstly prepare a polymeric replica that duplicates the surface morphology of a *S. apetala* leaf [24–26]. The antifouling performance of the replica is verified by attachment test with tubeworm larvae [27,28]. To gain deeper insights into the effects of surface morphology on antifouling performance, theoretical modelling is carried out, giving rise to guidelines for achieving better antifouling performance through morphology optimization. Finally, a biomimetic surface with microscopic ridge-like morphology is synthesized, showing comparable antifouling performance to that of the *S. apetala* leaves.

## 2. Polydimethylsiloxane replica of *Sonneratia apetala* leaves

To investigate the effect of surface morphology on antifouling performance and meanwhile mask other possible factors such as bioactive compounds, polydimethylsiloxane (PDMS) replicas of *S. apetala* leaves are prepared by a moulding process as illustrated in figure 2*a* (see Material and methodologies for detailed description). Figure 2*b*–*g* shows the surface morphology of a PDMS replica in comparison with that of the *S. apetala* leaf used for duplication. Clearly, the PDMS replica faithfully duplicates the microscopic ridge-like morphology of the *S. apetala* leaf, of which the height and thickness of the ridges are around 5 μm and 1 μm while the inter-ridge spacing is around 5 μm. Moreover, PDMS blocks with similar size but flat surfaces are also prepared as the control specimens for antifouling performance test.
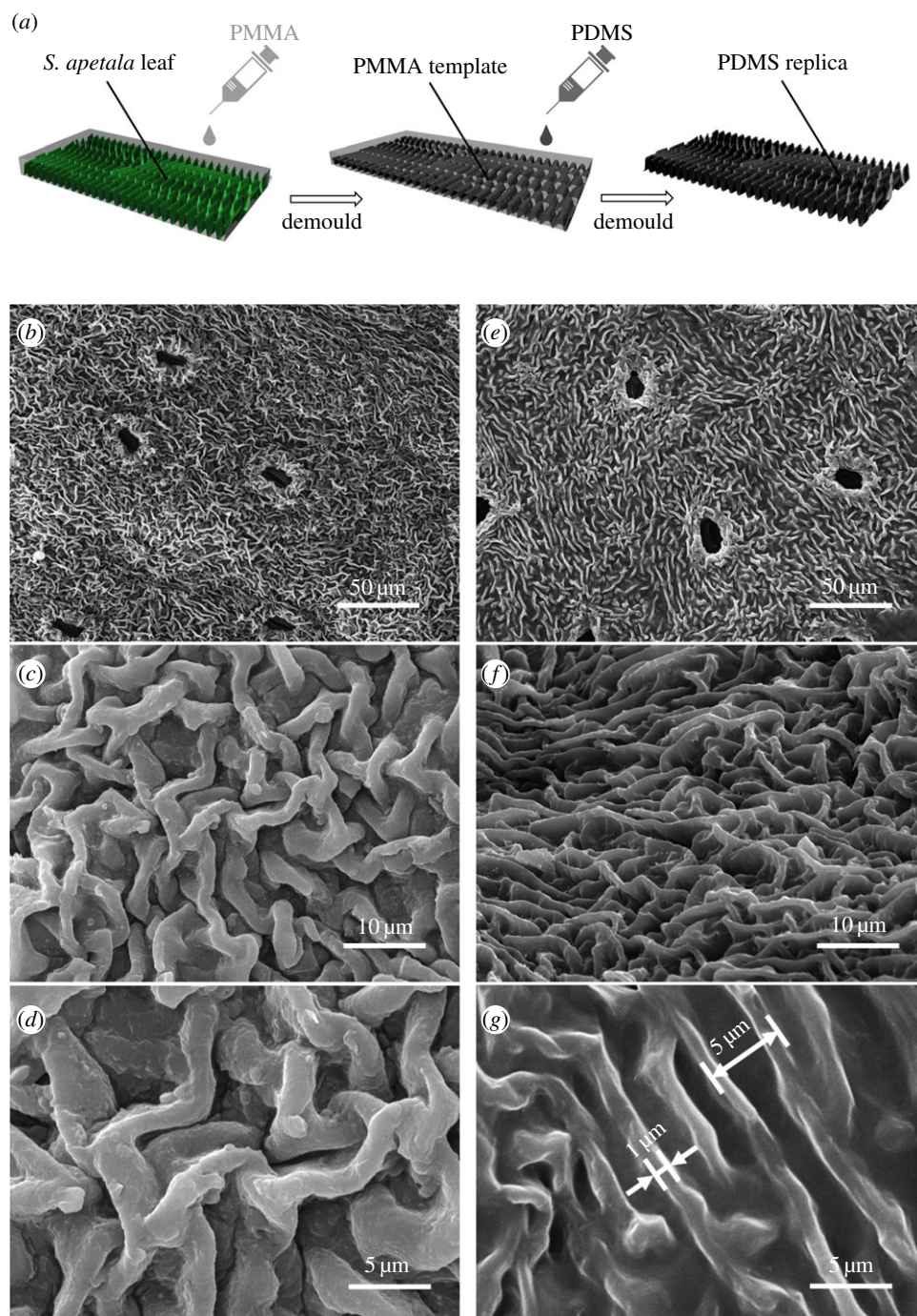
Figure 2. (*a*) Schematic of the moulding process for preparing PDMS replica of *S. apetala* leaves. (*b – d*) Scanning electron microscopy images of a leaf surface of *S. apetala* compared to (*e – g*) those of its replica.

To examine the antifouling performance of the PDMS replicas of the *S. apetala* leaves, settlement tests of tubeworms are carried out with flat PDMS samples and glass slides used as the controls (see Material and methodologies for details). Figure 3 shows the number of settled tubeworms on different surfaces after 24 h and 48 h immersion. It can be seen that little change happens in the number of settled tubeworms during the period from 24 h to 48 h, implying that the settlement of tubeworms mainly takes place within the first 24 h after immersion. This is most probably because the tubeworms that are unable to attach on the solid surfaces within 24 h will not survive for long. The number of tubeworms settled on the PDMS replicas after 24 h immersion is less than 5% of those on the flat PDMS surfaces and glass slides. Moreover, no significant difference in the numbers of attached tubeworms is observed between the flat PDMS surfaces and glass slides,

implying that surface morphology rather than material chemistry plays the dominant role in determining the settlement of tubeworms. This finding evokes an earlier similar study on the attachment of various fouling species on surfaces with microgrooves of different sizes [29]. It was concluded that the settlement of tubeworms on a textured surface is sensitive to the characteristic length scale of the texture. For a given type of texture, there exists an optimal characteristic length that can prohibit the settlement of tubeworms to the best extent. For the microscopic ridge-like surface morphology of *S. apetala* leaves, does the settlement of the tubeworms depend on its characteristic sizes? Are there any optimal characteristic lengths leading to better antifouling performance? To answer these questions, theoretical analysis is carried out to investigate the adhesion between a tubeworm and a surface with ridge-like morphology.
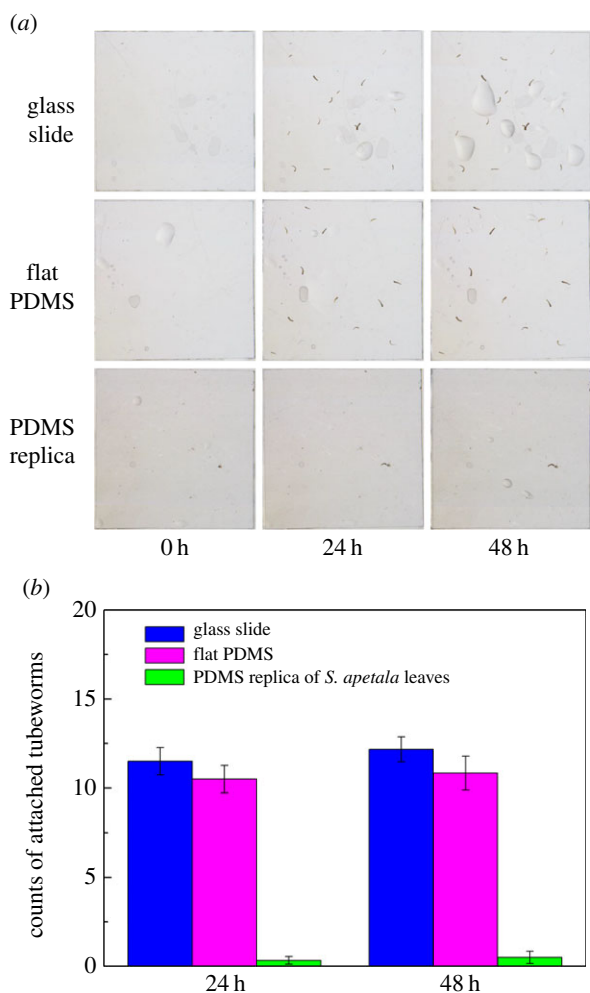
Figure 3. Antifouling performance of the PDMS replica of a *S. apetala* leaf. (*a*) Attachment of tubeworm larvae on glass slide, flat PDMS surface and PDMS replica of a *S. apetala* leaf after 0 h, 24 h and 48 h immersion. (*b*) Means $\pm$ s.e. ($n = 6$) of total counts of tubeworms attached on various surfaces after 24 h and 48 h.

3. Theoretical modelling

The effect of surface morphology on biofouling has long been recognized and studied [29–33]. One of the earliest theoretical attempts might be the attachment point theory, which indicated that textures with optimal characteristic sizes could prohibit the settlement of foulers. However, as an empirical description of the attachment of foulers on textured surfaces, the attachment point theory lacks physical basis, much less a quantitative estimation and prediction competence. To shed light on the size dependence of the antifouling performance of the ridge-like morphology, a quantitative model with physical basis, rigorous formulation and prediction competence is required.

For a tubeworm larva, we assume that the success rate of attachment on a textured surface depends on the maximum adhesion force that can be achieved between them. To quantify the adhesive force between a tubeworm and a textured surface shown in figure 2*b*, a mechanics model is established. Given the cylindrical shape of tubeworms and the microscopic ridge-like surface morphology of the *S. apetala* leaves, here we neglect the longitudinal dimension of the microscopic ridges and the disorder of their distribution and consider an adhesive contact problem between a two-dimensional (plane strain) cylinder and a substrate with wavy profile (figure 4*a*). Even though the fouling attachment involves complex chemical and biological processes, this simplified model is believed capable of capturing the mechanical essentials of fouling attachment.

Prior to solving the posed problem, it is worthwhile to introduce a useful result concerning the adhesion between an elastic cylinder and a flat substrate. Earlier studies indicated that the pull-off force between a cylinder (plane strain) and a flat substrate, which refers to the force required to separate them, is given by [34]

$$\left.\begin{array}{l} F_{\mathrm{pf}}^{\mathrm{Flat}} = 3\left(\dfrac{\pi E^* W^2 R_{\mathrm{T}}}{16}\right)^{1/3} \\[4mm] \text{with } E^* = \dfrac{1}{[(1 - \nu_{\mathrm{T}}^2)/E_{\mathrm{T}} + (1 - \nu_{\mathrm{S}}^2)/E_{\mathrm{S}}]}, \end{array}\right\} \tag{3.1}$$

where E_{T}, E_{S}, ν_{T}, ν_{S} denote the elastic moduli and Poisson's ratios of the cylinder and the substrate, respectively, R_{T} stands for the cross-sectional radius of the cylinder, and W represents the adhesion energy between the cylinder and substrate.

For a substrate with wavy profile, we assume that the profile is periodic and can be described by a trigonometric function $y = -A\cos(2\pi x/\lambda)$, where λ and A denote the wavelength and amplitude, two characteristic length scales of the profile, respectively. For simplicity, we assume $A = 0.5\lambda$ for the moment. Cases with other amplitudes will be discussed later. Consider a tubeworm, which is modelled as a cylinder, in contact with such a wavy substrate. Three types of stable configurations may occur, depending on the relative sizes between the tubeworm and the wavy profile. If the wavelength of the profile λ is much larger than the tubeworm's radius R_{T}, a stable configuration for the tubeworm is to rest on the trough of the groove, as shown in figure 4*a*(i). This configuration is called single-point attachment. Under this circumstance, the pull-off force is given by (see the electronic supplementary material for details)
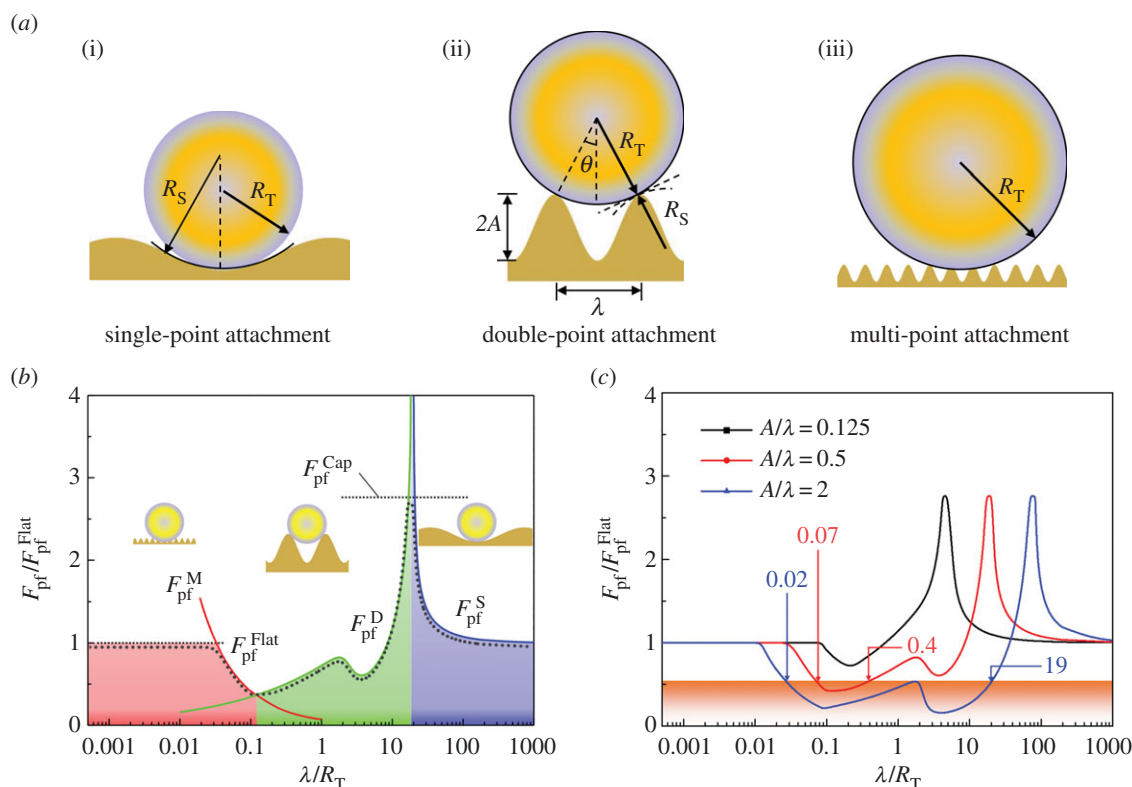
$$F_{\mathrm{pf}}^{\mathrm{S}} = \left(\frac{R_{\mathrm{S}}}{R_{\mathrm{S}} + R_{\mathrm{T}}}\right)^{1/3} F_{\mathrm{pf}}^{\mathrm{Flat}}, \tag{3.2}$$

where R_{S} represents the curvature radius at the trough of the substrate. Clearly, R_{S} as a function of λ can be derived from the profile function given above. Considering the concave profile at the trough of the profile, one has $R_{\mathrm{S}} \leq -R_{\mathrm{T}} < 0$ which implies that $F_{\mathrm{pf}}^{\mathrm{S}} > F_{\mathrm{pf}}^{\mathrm{Flat}}$. It can be noticed that the pull-off force given in equation (3.2) goes to infinity when $R_{\mathrm{S}} = -R_{\mathrm{T}}$. Such unrealistic singularity is essentially attributed to the conventional parabolic approximation for circular profile in contact mechanics [34]. A reasonable cap of the pull-off force under the circumstance with $R_{\mathrm{S}} = -R_{\mathrm{T}}$ is estimated to be (see the electronic supplementary material for details)

$$F_{\mathrm{pf}}^{\mathrm{Cap}} = 1.19\left(\frac{\pi E^* R_{\mathrm{T}}}{W}\right)^{1/6} F_{\mathrm{pf}}^{\mathrm{Flat}}. \tag{3.3}$$

For the profile with intermediate wavelength λ, the spacing between two adjacent ridges is too narrow to accommodate a tubeworm at the trough. For stable attachment, a tubeworm has to straddle over a groove between two adjacent ridges, forming a configuration called double-point attachment (figure 4*a*(ii)). In this circumstance, the pull-off force is given by (see the electronic supplementary material for details)

$$F_{\mathrm{pf}}^{\mathrm{D}} = 2\cos\theta \cdot \left(\frac{R_{\mathrm{S}}}{R_{\mathrm{S}} + R_{\mathrm{T}}}\right)^{1/3} F_{\mathrm{pf}}^{\mathrm{Flat}}, \tag{3.4}$$

Figure 4. (a) Schematic of three possible configurations of an elastic cylinder in adhesive contact with a wavy substrate. (b) Variation of the normalized pull-off force with λ/R_T for $A/\lambda = 0.5$. (c) Effect of A/λ on pull-off force.

where R_S represents the curvature radius of the substrate at the contact points, and θ is the contact angle designated in figure 4a(ii). Basic geometrical relations indicate that R_S and θ are both functions of R_T and λ, so does F_{pf}^D.

If the characteristic size of the profile λ is much smaller than the size of the tubeworm, more than two contact points will form between the tubeworm and substrate, giving rise to a multi-point attachment configuration, as shown in figure 4a(iii). In that case, an approximate solution to the pull-off force is given by (see electronic supplementary material for details)

$$F_{pf}^M = \left(\frac{2}{\pi}\right)^{10/9} \left(\frac{W}{2\pi E^* R_T}\right)^{4/9} \left(\frac{\lambda}{A}\right)^{5/9} \left(\frac{\lambda}{R_T}\right)^{-7/9} \cdot F_{pf}^{Flat}. \quad (3.5)$$

Nevertheless, equation (3.5) is applicable only to λ in a limited range because F_{pf}^M will go to infinity as λ approaches zero. Such unrealistic singularity is attributed to the neglect of the interaction between different contact points in our estimation (see the electronic supplementary material). Clearly, the wavy substrate will become flat and smooth as λ approaches zero. That is, F_{pf}^M should asymptotically approach F_{pf}^{Flat} as λ approaches zero.

Equations (3.2)–(3.5) comprise the whole picture of the variation of pull-off force with the characteristic length scale of surface profile, λ, as depicted in figure 4b. It can be seen that the pull-off force between a tubeworm and a rough surface could be either higher or lower than that on a flat surface, depending on the characteristic length scale of surface roughness. For a surface with sinusoidal profile as we assumed, the maximum pull-off force occurs when the wavelength λ is around 10 times of the tubeworm's diameter. The magnitude of the maximum pull-off force is proportional to $(W/\pi E^* R_T)^{1/6}$. The minimum pull-off force, which takes

place when $\lambda/R_T = 0.1$ is less than 45% of F_{pf}^{Flat}, implying the best antifouling performance of a profile with $\lambda = 0.1\,R_T$.

The analysis carried out so far is for a given ratio of $A/\lambda = 0.5$. To investigate the effects of profile amplitude A on the pull-off force, similar analysis is performed by taking $A/\lambda = 0.125$ and 2.0. Figure 4c compares the variations of the pull-off force as a function of λ/R_T for these three cases. When $A/\lambda = 0.125$, there is only a small range of λ/R_T giving pull-off force less than F_{pf}^{Flat} with minimum value around 0.7 F_{pf}^{Flat}. With increase of A/λ, the range of λ/R_T that gives rise to relatively lower pull-off force expands. When $A/\lambda = 0.5$, the range of λ/R_T in which the pull-off force is less than 0.5 F_{pf}^{Flat} is 0.07–0.4. Such range extends to 0.02–19 when $A/\lambda = 2$. Considering the diversity of tubeworms in size, above results imply that high ridges can tackle the fouling of tubeworms of different sizes better. For *S. apetala* leaves and their PDMS replicas, the inter-ridge spacing is around 5 μm which is around 10% of the radius of a tubeworm larva (approx. 50 μm). In the light of figure 4b,c, such ratio of λ/R_T should give rise to a lower pull-off force and therefore better antifouling performance as confirmed by the attachment tests above. Additionally, figure 4b,c also implies practical guidelines for the design of antifouling surface with ridge-like morphology. That is, high ridges, and proper inter-ridge spacing should be adopted.

4. Synthetic antifouling surface with microscopic ridge-like morphology

Above theoretical modelling indicates that high ridges with appropriate inter-ridge spacing are crucial for better antifouling performance. To further verify this finding and overcome the size limitation of replica of the natural antifouling surfaces, a synthetic surface with microscopic ridge-like morphology is prepared by water bath method with graphite
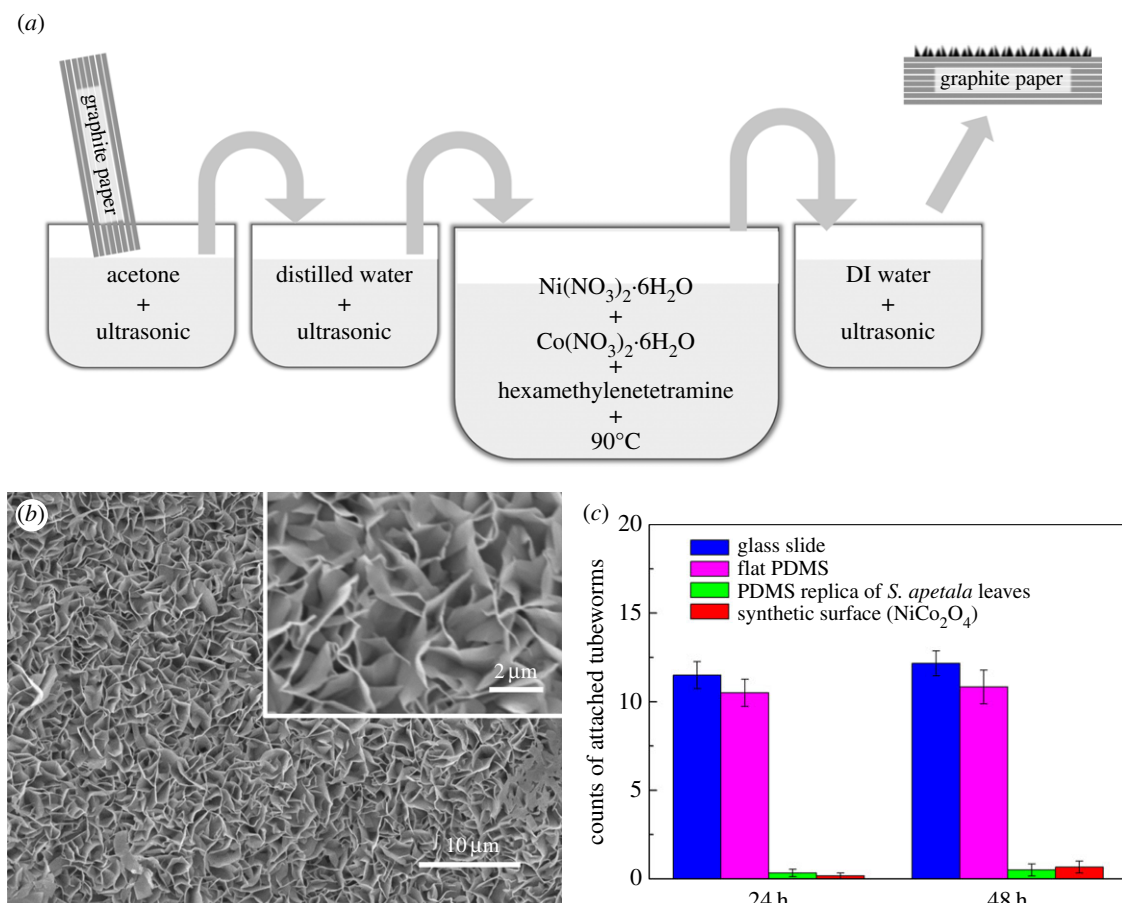
Figure 5. (a) Schematic of the synthesis process of antifouling surface. (b) Scanning electron microscopy images of a synthetic surface with microscopic ridge-like morphology. (c) Means $\pm$ s.e. ($n = 6$) of the total counts of tubeworms attached on the synthetic surfaces with microscopic ridge-like morphology.

paper (GP) in aqueous solution containing nickel and cobalt nitrates (figure 5a and Material and methodologies). Figure 5 shows the scanning electron microscopy images of the obtained surface which is covered with nanoflakes vertically situated on the underlying graphite substrate, giving rise to microscopic ridge-like morphology similar to that of the *S. apetala* leaves. The nanoflakes, which are identified as $NiCo_2O_4$, are around tens of nanometres in thickness and a few micrometres in lateral dimensions. The inter-ridge spacing ranges from several hundred nanometres to several micrometres. The ratios of λ/R_T and A/λ are estimated to be in the ranges of 0.01–0.1 and 2–20, respectively, which, according to figure 4b,c, implies great antifouling potential. Settlement test with tubeworm larvae is also carried out for such synthetic ridge-like surfaces. The numbers of the settled tubeworms after 24 h and 48 h immersion are less than 10% of those on the glass slides and flat PDMS surfaces, as shown in figure 5c. Such outstanding antifouling performance is comparable with that of the PDMS replica of the *S. apetala* leaves. Certainly, for a practical antifouling application, such $NiCo_2O_4$ nanoflake coating is still at the embryo stage. Its mechanical robustness and drag force in flow fields would be the topics of interest for further investigation.

5. Conclusion

Inspired by the superior antifouling performance of *S. apetala* leaves, in this work we investigated the effect of surface morphology on antifouling performance. It was demonstrated that the excellent antifouling performance of the *S. apetala*

leaves can be attributed to their microscopic ridge-like surface morphology. Theoretical modelling further indicated that high ridge and proper inter-ridge spacing would reduce the attachment probability of foulers and therefore facilitate antifouling. According to this guidance, a biomimetic surface with microscopic ridge-like morphology was synthesized. The follow-up attachment tests reconfirmed the feasibility of using ridge-like surface morphology to control biofouling. As a preliminary study, our present work mainly focused on the size effect of surface morphology, while the disorder effect of the microscopic ridge-like pattern was neglected for the moment. Such idealization allowed us to investigate the size effect of the morphology analytically. It is evident that the pull-off force between the fouler and substrate also depends on the disorder degree of the pattern, mechanical properties and adhesion energy of the substrate. The quantitative effects of these factors on the antifouling performance are still unclear and expected for in-depth investigations. Moreover, in our current study we applied tubeworms to test the antifouling performance. The applicability of the current microscopic ridge-like morphology to other fouling species remains unclear and deserves further study.

6. Material and methodologies

6.1. Preparation of polydimethylsiloxane replicas of *Sonneratia apetala* leaves

Firstly, the *S. apetala* leaves were cleaned using acetone and dried in air. Then, a poly(methyl methacrylate) (PMMA)

solution (acetone as solvent) was poured directly onto a treated leaf's surface. After curing of the PMMA, the leaf was peeled off from the PMMA, giving rise to a negative PMMA mould duplicating the morphology of the leaf. Then, PDMS base and cross-linker were mixed in a volume ratio of $10 : 1$. The obtained mixture was poured onto the negative PMMA mould in a glass dish. The whole set was placed in a desiccator for low-pressure degassing for 1 h. After curing at room temperature for 48 h, the PDMS replica was obtained after demoulding from the PMMA mould.

6.2. Attachment test with tubeworm larvae

Prior to test, all surface specimens to be tested were immersed into sterile deionized water for sufficient wetting. Then the wetted specimens were placed into a petri dish, which contained 20 ml seawater and around 100 tubeworm larvae (approx. 100 μm in width, approx. 300 μm in length; see electronic supplementary material for the culturing details). To ensure the repeatability of the results to be obtained, six replicas were prepared in parallel. All the test groups were kept in an ambient environment for 48 h in a $12 \, L : 12 \, D$ cycle. During the test process, the settled tubeworms were counted carefully with the aid of an optical microscope at 24 h and 48 h. All the specimens were dip-rinsed three times in filtered seawater to remove any unsettled tubeworms if available.

6.3. Synthesis of biomimetic antifouling surface

A piece of GP with size of $20 \times 40 \times 0.5$ mm (width $\times$ length $\times$ thickness) was rinsed with acetone and distilled (DI) water, and then dried in a vacuum oven overnight at 80°C. The treated GP was then immersed into a solution made by dissolving 0.5 mmol $Ni(NO_3)_2 \cdot 6H_2O$, 1 mmol $Co(NO_3)_2 \cdot 6H_2O$ and 2.2 mmol hexamethylenetetramine into 20 ml DI water and 10 ml ethanol. The solution together with GP was transferred to a Teflon-lined stainless-steel autoclave and kept at 90°C for 6 h. After cooling down to room temperature, the GP covered with $NiCo_2O_4$ nanoflakes was obtained, which was ready for antifouling test after thorough rinsing with DI water and ethanol followed by drying at 60°C for 12 h.

References

1. Callow JA, Callow ME. 2011 Trends in the development of environmentally friendly fouling-resistant marine coatings. *Nat. Commun.* **2**, 244. (doi:10.1038/ncomms1251)

2. Schultz MP. 2007 Effects of coating roughness and biofouling on ship resistance and powering. *Biofouling* **23**, 331–341. (doi:10.1080/08927010701461974)

3. Hall-Stoodley L, Costerton JW, Stoodley P. 2004 Bacterial biofilms: from the natural environment to infectious diseases. *Nat. Rev. Microbiol.* **2**, 95–108. (doi:10.1038/nrmicro821)

4. Clare AS. 1996 Marine natural product antifoulants: status and potential. *Biofouling* **9**, 211–229. (doi:10.1080/08927019609378304)

5. Qian PY, Rittschof D, Sreedhar B. 2000 Macrofouling in unidirectional flow: miniature pipes as experimental models for studying the interaction of flow and surface characteristics on the attachment of barnacle, bryozoan and polychaete larvae. *Mar. Ecol. Prog. Ser.* **207**, 109–121. (doi:10.3354/meps207109)

6. Tesler AB, Kim P, Kolle S, Howell C, Ahanotu O, Aizenberg J. 2015 Extremely durable biofouling-resistant metallic surfaces based on electrodeposited nanoporous tungstite films on steel. *Nat. Commun.* **6**, 8649. (doi:10.1038/ncomms9649)

7. Rosenhahn A, Ederth T, Pettitt ME. 2008 Advanced nanostructures for the control of biofouling: the FP6 EU Integrated Project AMBIO. *Biointerphases* **3**, 1–5. (doi:10.1116/1.2844718)

8. Champ MA. 2000 A review of organotin regulatory strategies, pending actions, related costs and benefits. *Sci. Total Environ.* **258**, 21–71. (doi:10.1016/s0048-9697(00)00506-4)

9. Yebra DM, Kiil S, Dam-Johansen K. 2004 Antifouling technology—past, present and future steps towards efficient and environmentally friendly antifouling coatings. *Prog. Org. Coat.* **50**, 75–104. (doi:10.1016/j.porgcoat.2003.06.001)

10. Almeida E, Diamantino TC, de Sousa O. 2007 Marine paints: the particular case of antifouling paints. *Prog. Org. Coat.* **59**, 2–20. (doi:10.1016/j.porgcoat.2007.01.017)

11. Voulvoulis N, Scrimshaw MD, Lester JN. 2002 Comparative environmental assessment of biocides used in antifouling paints. *Chemosphere* **47**, 789–795. (doi:10.1016/s0045-6535(01)00336-8)

12. Ralston E, Swain G. 2009 Bioinspiration—the solution for biofouling control? *Bioinspir. Biomim.* **4**, 015007. (doi:10.1088/1748-3182/4/1/015007)

13. Bixler GD, Bhushan B. 2012 Biofouling: lessons from nature. *Phil. Trans. R. Soc. A* **370**, 2381–2417. (doi:10.1098/rsta.2011.0502)

14. Cordeiro AL, Werner C. 2011 Enzymes for antifouling strategies. *J. Adhes. Sci. Technol.* **25**, 2317–2344. (doi:10.1163/016942411X574961)

15. Dobretsov S, Dahms H-U, Qian P-Y. 2006 Inhibition of biofouling by marine microorganisms and their metabolites. *Biofouling* **22**, 43–54. (doi:10.1080/08927010500504784)

16. Falconnet D, Csucs G, Grandin HM, Textor M. 2006 Surface engineering approaches to micropattern surfaces for cell-based assays. *Biomaterials* **27**, 3044–3063. (doi:10.1016/j.biomaterials.2005.12.024)

17. Du T, Ma SH, Pei XW, Wang ST, Zhou F. 2017 Bio-inspired design and fabrication of micro/nano-brush dual structural surfaces for switchable oil adhesion and antifouling. *Small* **13**, 1602020. (doi:10.1002/smll.201602020)

18. Shivapooja P, Wang Q, Orihuela B, Rittschof D, Lopez GP, Zhao X. 2013 Bioinspired surfaces with dynamic topography for active control of biofouling. *Adv. Mater.* **25**, 1430–1434. (doi:10.1002/adma.201203374)

19. Brzozowska AM, Parra-Velandia FJ, Quintana R, Zhu XY, Lee SSC, Chin-Sing L, Janczewski D, Teo SLM, Vancso JG. 2014 Biomimicking micropatterned surfaces and their effect on marine biofouling. *Langmuir* **30**, 9165–9175. (doi:10.1021/la502006s)

20. Schumacher JF, Aldred N, Callow ME, Finlay JA, Callow JA, Clare AS, Brennan AB. 2007 Species-specific engineered antifouling topographies: correlations between the settlement of algal zoospores and barnacle cyprids. *Biofouling* **23**, 307–317. (doi:10.1080/08927010701393276)

21. Cao XY et al. 2010 Interaction of zoospores of the green alga *Ulva* with bioinspired micro- and nanostructured surfaces prepared by polyelectrolyte layer-by-layer self-assembly. *Adv. Funct. Mater.* **20**, 1984–1993. (doi:10.1002/adfm.201000242)

22. Wan F, Pei XW, Yu B, Ye Q, Zhou F, Xue QJ. 2012 Grafting polymer brushes on biomimetic structural

surfaces for anti-algae fouling and foul release. *ACS Appl. Mater. Interfaces* **4**, 4557–4565. (doi:10.1021/am300912w)

23. Feng DQ, Wang W, Wang X, Qiu Y, Ke CH. 2016 Low barnacle fouling on leaves of the mangrove plant *Sonneratia apetala* and possible anti-barnacle defense strategies. *Mar. Ecol. Prog. Ser.* **544**, 169–182. (doi:10.3354/meps11585)

24. Ismail AE, Grest GS, Heine DR, Stevens MJ, Tsige M. 2009 Interfacial structure and dynamics of siloxane systems: PDMS–vapor and PDMS–water. *Macromolecules* **42**, 3186–3194. (doi:10.1021/ma802805y)

25. Efimenko K, Finlay J, Callow ME, Callow JA, Genzer J. 2009 Development and testing of hierarchically wrinkled coatings for marine antifouling. *ACS Appl. Mater. Interfaces* **1**, 1031–1040. (doi:10.1021/am9000562)

26. Banerjee I, Pangule RC, Kane RS. 2011 Antifouling coatings: recent developments in the design of surfaces that prevent fouling by proteins, bacteria,

and marine organisms. *Adv. Mater.* **23**, 690–718. (doi:10.1002/adma.201001215)

27. Shikuma NJ, Pilhofer M, Weiss GL, Hadfield MG, Jensen GJ, Newman DK. 2014 Marine tubeworm metamorphosis induced by arrays of bacterial phage tail-like structures. *Science* **343**, 529–533. (doi:10.1126/science.1246794)

28. Hadfield MG, Nedved BT, Wilbur S, Koehl MAR. 2014 Biofilm cue for larval settlement in *Hydroides elegans* (Polychaeta): is contact necessary? *Mar. Biol.* **161**, 2577-2587. (doi:10.1007/s00227-014-2529-0)

29. Scardino AJ, Guenther J, de Nys R. 2008 Attachment point theory revisited: the fouling response to a microtextured matrix. *Biofouling* **24**, 45–53. (doi:10.1080/08927010701784391)

30. Decker JT, Sheats JT, Brennan AB. 2014 Engineered antifouling microtopographies: surface pattern effects on cell distribution. *Langmuir* **30**, 15 212–15 218. (doi:10.1021/la504215b)

31. Decker JT, Kirschner CM, Long CJ, Finlay JA, Callow ME, Callow JA, Brennan AB. 2013 Engineered antifouling microtopographies: an energetic model that predicts cell attachment. *Langmuir* **29**, 13 023–13 030. (doi:10.1021/la402952u)

32. Scardino AJ, Harvey E, De Nys R. 2006 Testing attachment point theory: diatom attachment on microtextured polyimide biomimics. *Biofouling* **22**, 55–60. (doi:10.1080/08927010500506094)

33. Brzozowska AM, Maassen S, Rong RGZ, Benke PI, Lim CS, Marzinelli EM, Janczewski D, Teo SLM, Vancso GJ. 2017 Effect of variations in micropatterns and surface modulus on marine fouling of engineering polymers. *ACS Appl. Mater. Interfaces* **9**, 17 509–17 517. (doi:10.1021/acsami.6b14262)

34. Chaudhury MK, Weaver T, Hui CY, Kramer EJ. 1996 Adhesive contact of cylindrical lens and a flat sheet. *J. Appl. Phys.* **80**, 30–37. (doi:10.1063/1.362819)